Journal of Astronomical Instrumentation

The Effects of the Local Environment on a Compact Radio Interferometer: Cross-coupling and ground pickup in the Tianlai Dish Pathfinder Array

Juhun (David) Kwak[1], Albert Stebbins[2], Haotian Cao[1], John Podczerwinski[1], Peter Timbie[1,7], Reza Ansari[3], John Marriner[2], Xuelei Chen[4,5,6], Jixia Li[4,5], Fengquan Wu[4], and other authors who wish to "opt-in"
[1] *Department of Physics, University of Wisconsin – Madison, Madison, Wisconsin 53706, USA*
[2] *Fermi National Accelerator Laboratory, P.O. Box 500, Batavia IL 60510, USA*
[3] *Université Paris-Saclay, CNRS/IN2P3, IJCLab, 91405 Orsay, France*
[4] *National Astronomical Observatory, Chinese Academy of Sciences, 20A Datun Road, Beijing 100101, China*
[5] *University of Chinese Academy of Sciences, Beijing 100049, China*
[6] *Center of High Energy Physics, Peking University, Beijing 100871, China*

Received (to be inserted by publisher); Revised (to be inserted by publisher); Accepted (to be inserted by publisher);

Abstract: The visibilities measured by radio astronomical interferometers include non-astronomical correlated signals that arise from the local environment of the array. These correlated signals increase in compact arrays such as those under development for 21 cm intensity mapping. The amplitude of the contaminated visibilities exceeds the size of the signal expected from the 21 cm signal alone and represents a significant systematic effect. We study two sources of such correlated signals: receiver noise radiated by each antenna that couples to the other antennas; and thermal radiation from the ground in the vicinity of the array that couples into the antennas and produces non-zero visibilities. We develop a model for these effects and apply it to the Tianlai Dish Pathfinder Array, a compact array of 16, 6-m dish antennas, using electromagnetic simulations. We compare the model to drift-scan observations with the array and set requirements on the level and stability of antenna cross-coupling and sidelobes for future 21 cm intensity mapping instruments.

Keywords: 21 cm intensity mapping; local noise; cross-coupling; ground pickup.

1. Color Coding

red: citation
purple: wording/phrasing
orange: changes
blue: to-dos, needs attention

2. Introduction (David; Peter)

21 cm intensity mapping is a technique for measuring the large scale structure of the universe using the redshifted 21 cm line from neutral hydrogen gas (HI) (Liu & Shaw 2020; Morales & Wyithe 2010). It is an example of the general case of line intensity mapping (Kovetz et al. 2019), in which spectral lines from any species, such as CO and CII, are used to make three-dimensional, "tomographic" maps of large cosmic volumes. 21 cm intensity mapping is used to study the formation of the first objects during the Cosmic Dawn and the Epoch of Reionization ($6 \leq z \leq 50$) and for addressing other cosmological questions with observations in the post-reionization epoch ($z \leq 6$), such as constraining inflation models (Xu et al. 2016) and the equation of state of dark energy (Xu et al. 2015). In the latter epoch, the approach provides an attractive alternative to galaxy redshift surveys. It measure the collcetive emission from many haloes simultaneously, both bright and faint, rather than cataloging just the brightest objects. As a result,

[7] pttimbie@wisc.edu

the required angular resolution is relaxed as individual galaxies do not need to be resolved. By observing with wide-band receivers one simultaneously obtains signals over a range of redshifts and can construct a tomographic map. The primary analysis tool for cosmological measurements is the three-dimensional power spectrum of a natural means to compute this spectrum over a range of wave numbers, k, in which the perturbations are in the linear regime. Of particular interest in the power spectrum are the baryon acoustic oscillation (BAO) features, which can be used as a cosmic ruler for studying the expansion rate of the universe as a function of redshift.

21 cm intensity mapping, however, is challenging for various reasons, with the primary concern being that the HI signal is orders of magnitude weaker than the noise sources. This makes the calibration of the noise particularly significant. The biggest contribution for such noises is from the galactic and extragalactic foreground, which is difficult to remove accurately. This, on the other hand, is studied more extensively compared to the noises due to the local environment at the observation sites. While it is important to understand and remove the foreground noise, we recognize that understanding the local noises is crucial for the 21 cm intensity mapping experiments to achieve the scientific goals concerning cosmology, as it may mask the detail structure of the signals. Here, we will address the noise due to the reradiation of the signals from the electric dipoles at the antennas, which we refer to as cross-coupling, and the noises due to the radiation from ground among the noises due to the local environment. We attempt to simulate these noises electromagnetically and compare it to the observational data and the other rather direct measurements of cross-coupling from the Tianlai Dish Pathfinder Array, to provide a model and a calibration strategy for such noises. We hope that our methods and findings are sufficiently general and efficient, that they, with some appropriate modification, could be applied to any future line intensity mapping experiments using the ground-based radio interferometers.

In a conventional radio interferometer, the effect of cross-coupling is negligible as each of the telescope is sufficiently far apart from the others, motivated by the increased resolution that scales as the baseline length. In contrast, in the case of the interferometer built for 21 cm intensity mapping, the array is much more compact. This is because we are not so interested in the detailed structure of the power spectrum, but the relatively faint signals from large structures, which require a high sensitivity. Consequently, the correlated noise has a much bigger impact to the observations with a 21 cm intensity mapping array like Tianlai. This is difficult to calibrate as its level is similar to the signals of interests in general, which not only is high in magnitude but also adds structures to the spectrum. Naturally, understanding cross-coupling is crucial to the calibration of the data and thus understanding the signals of interests. Our analysis suggests that this is particularly important in extracting the cosmological information from the data such as the power spectrum, which may be used as a probe of inflation. Preceding works on this topic exist, but are somewhat limited in terms of both scope and depth. The contributions primarily come from the Hydrogen Epoch of Reionization Array (HERA) collaboration. HERA collaboration has addressed the correlated noise with a finite impulse response high-pass filter (Kern *et al.*, 2019) and with the combination of Fourier techniques and matrix analysis (Kern *et al.*, 2020) as a part of a more general attempt to remove the noise. Although they successfully remove some features in the signals that are considered noise, they have not provided satisfying insights into where the noises could have come from. Later, they attempt to further their analysis on correlated noise through CST simulations (Fagnoni *et al.*, 2021). Still, the main focus of the paper laid on the sky signals that are received at the feed after bouncing off the elements of the other dishes in the array. See also (Josaitis *et al.*, 2022) for an analysis of cross-coupling in HERA.

Introduce ground pickup effects here (Peter will attempt to summarize Albert's analysis.).

This paper is organized as follows: in Sect. 3, we summarizes the characteristics of the Tianlai Dish Pathfinder Array and further motivate our analysis by referring to our preceding works. In Sect. 4, we describe our models for noises due to cross-coupling and ground pickup. In Sect. 5, we introduce the properties of CST Studio Suite, an electromagnetic simulation software that we use, and how we performed our simulations. In Sect. 6, we presents our results from the cross-coupling simulations with our analysis and interpretation. In Sect. 7, results from the ground pickup simulation is presented. Then, in Sect. 8, we combine all our simulations together along with the sky simulation that simulates the noise contribution from the astronomical sources and compare it with the nightly mean visibility, which we believe is dominated

by noise. After these, we present methods to mitigate the effect of such noises in Sect. 9 and conclude with conclusions in Sect. 10. There are also two appendices that elaborate on the model for emissivity (App. 1) which is important in investigating the ground pickup and the model for the receiver noise (App. B).

3. Tianlai Dish Array (David)

Review 'correlated noise' results from (Wu *et al.*, 2021) for 10 nights, comparison to expected signal.

Tianlai program aims to make a 21 cm intensity mapping survey of the northen sky. At present the Tianlai program is in its Pathfinder stage to test the technology for making 21 cm intensity mapping observations with an interferometer array. The Pathfinder comprises of two arrays, one with 16 dish antennas and the other with cylinder reflectors antennas, located next to each other at a radio quiet site (44°9'N, 91°48'E) in Hongliuxia, Balikun County, Xinjiang Autonomous Region, in northwest China. We summarize below the design of the dish array for the present purposes. More details about the instruments can be found in (Wu *et al.*, 2021).

The feed antennas, amplifiers, and reflectors are designed to operate from 400 MHz to 1430 MHz, corresponding to HI at the redshift of $2.55 \geq z \geq -0.01$. The instrument can be tuned to operate in an RF bandwidth of 100 MHz, centered at any frequency in this range by adjusting the local oscillator frequency in the receivers and replacing the band pass filters. Currently, the Pathfinder operates at 700 - 800 MHz, corresponding to $1.03 \geq z \geq 0.78$. Future observations are planned in the 1330 - 1430 MHz band ($0.07 \geq z \geq -0.01$) to facilitate cross correlation with low-z galaxy redshift surveys and other low-z HI surveys. The dish array consists of 16 on-axis dishes. Each has an aperture of 6 m. The design parameters of the dishes are presented in Table **??**. The dishes are equipped with dual, linear-polarization receivers, and are mounted on Alt-Azimuth mounts. One polarization axis is oriented parallel to the altitude axis (horizontal, H, parallel to the ground) and the other is orthogonal to that axis (vertical, V) (Zhang et al. 2020). Motors are used to control the dishes electronically. The motors can steer the dishes to any direction in the sky above the horizon. The drivers are not specially designed for tracking celestial targets with high precision. Instead, in the normal observation mode, we point the dishes at a fixed direction and perform drift scan observations. The Alt-Azimuth drive provides flexibility during commissioning for testing and calibration. The dish array was fabricated by CASIC-23.

The dishes are currently arranged in a circular cluster. The array is roughly close-packed, with center-to-center spacings between neighboring dishes of approximately 8.8 m. The spacing is chosen to allow the dishes to point down to elevation angles as low as 35° without "shadowing" each other. ONe antenna is positioned at the center and the remaining 15 antennas are arranged in two concentric circles around it. It is well known that the baselines of circular array configurations are quite independent and have wide coverage of the (u, v) plane. A comparison of the different configurations considered for the Tianlai Dish Array and the performance of the adopted configuration can be found in (Zhang et al. 2016b). The Tianlai dishes are lightweight and the mounts are detachable, which enables the rearrangement of the antennas if needed. This paper describes observations with the current configuration.

4. Models (David; Albert)

Thermal noise, S21. See cylinder cross-coupling paper (Sun *et al.*, 2022) for an electrical model for receiver noise. See also (Padin *et al.*, 2000, 2002) model for the CBI instrument.

4.1. *Coupling model*

$$\begin{bmatrix} V_1^- \\ V_2^- \\ \vdots \\ V_N^- \end{bmatrix} = \begin{bmatrix} S_{11} & S_{12} \cdots & S_{1N} \\ S_{21} & & \vdots \\ \vdots & & \vdots \\ S_{N1} & \cdots \cdots & S_{NN} \end{bmatrix} \begin{bmatrix} V_1^+ \\ V_2^+ \\ \vdots \\ V_N^+ \end{bmatrix} \tag{1}$$

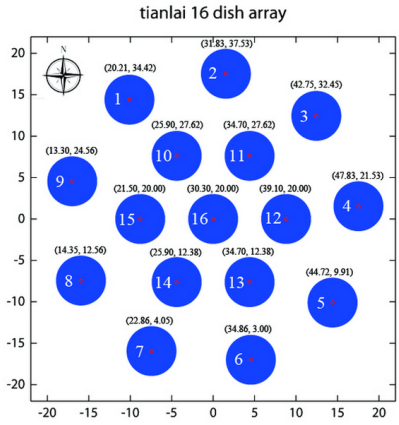

Fig. 1. Caption

Then, a specific element of the scattering matrix can be found by

$$S_{ij} = \frac{V_i^-}{V_j^+}\Big|_{V_k^+=0 \text{ for } k\neq j} \tag{2}$$

4.2. *Albert's model for ground pickup (Albert)*

See Fig. 2.

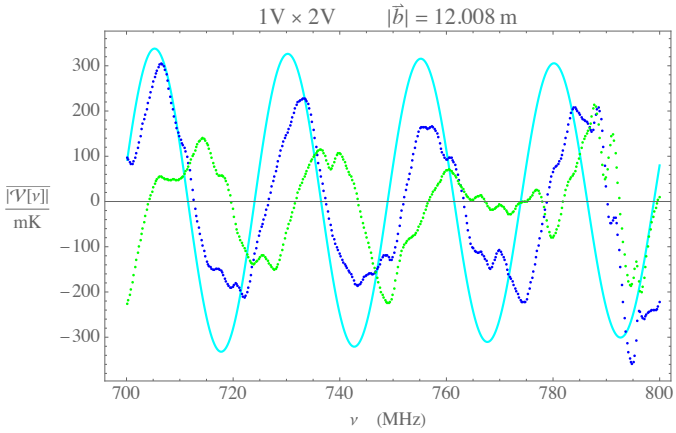

Fig. 2. Simulated and measured ground pickup from baseline 1V-2V. Dark blue and light blue curves are the real and imaginary parts of the ground signal, respectively. Cyan is the simulated ground signal, assuming...

5. Electromagnetic Simulations (David)

5.1. *CST simulations of S-parameters*

To simulate the effect of cross-coupling, we use CST Studio Suite. CST is an electromagnetic simulation software capable of running different simulations involving many electromagnetic devices including antennae. We simulate the response of a port of interest to the signal radiated from one of the other ports of the antennae in the array. Users can access two different types of cross-coupling data in CST, namely amplitude coupling and power coupling. The amplitude coupling is the ratio of the amplitudes of the emitted and received voltage signal while the power coupling is the ratio of powers between the emitted and received signal. Therefore, the amplitude coupling and power coupling are related as follow. Suppose the amplitude

coupling for a given frequency is $A = a + bi$. Then, the power coupling for the given frequency is

$$P = 20 \log_{10} \left(\sqrt{a^2 + b^2} \right) \tag{3}$$

CST simulates the amplitude coupling and convert the result to power coupling to present it in decibel as default. The users can still access the amplitude coupling data by choosing the real/imaginary options in the 1D result tap.

In order to simulate the cross-coupling with all elements of the array present, we include all dishes and ports in the array. On the other hand, only the port of interests, namely 2V and 10V, are selected to be excited. This is to minimize the simulation time without sacrificing the results necessary to investigate the S-parameter symmetry, distance dependency and the direction vector dependency of the cross-coupling. The particular ports are chosen since the result presented in Fig.26 of (cite first result paper) is from the 2V-10V baseline. In this paper, the correlated noise of 10Vx2V, 15Vx2V and 8Vx2V are analyzed in detail as highlighted by Fig. 3. These results should be sufficient to investigate the cross-coupling dependence on the separation between the pair of dishes.

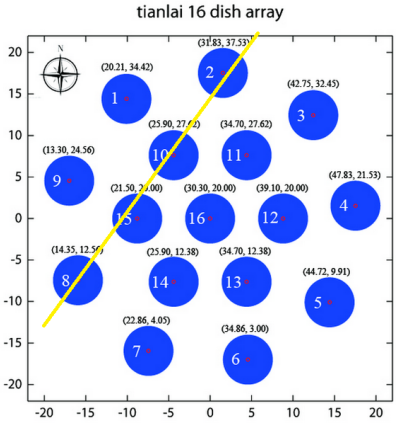

Fig. 3. Baselines whose cross-coupling is analyzed in detail in this paper. V, stands for vertical, represents the North-South polarization of the port, or the E-plane.

There are two different types of ports available in CST studio for excitation signal, namely waveguide port and discrete port. For the simulation of the cross-coupling effect, the use of waveguide port is appropriate since the reflection from the dishes can be reduced greatly. This is because the waveguide port extend through the dish model and to the infinity of the direction to which it is set up, whereas discrete port has finite length, which results in reflections of the signals from the structures under the lower end of the port. There are various types of solvers that solve problems with different techniques in CST. We experiment with two of them: the Transient Solver and Integral Equation Solver (IES). This is to check whether the results of the simulations are sensible and match each other. In addition, we can decide which solver is more efficient in solving the problem of interest.

The Transient Solver is based on the Finite Integration Technique. It applies numerical methods like the Perfect Boundary Approximation and the Thin Sheet Technique. These techniques allow for robust meshing in return for efficient memory usage. The use of the Transient Solver is motivated by (cite Fagnoni) as it is used for the analysis of reflections from the HERA array. Yet, the method was not suitable for simulating cross-coupling of the Tianlai dish array since the array is radially symmetric instead of being symmetric to a line of reference. Moreover, the difference in observing frequencies, namely 50 MHz $\sim$ 250 MHz for HERA citation? and 700 MHz $\sim$ 800 MHz for Tianlai for the observation presented in (cite first result paper), results in much more mesh cells for our simulations as the general meshing properties is determined by maximum number of cells per wavelength, and higher frequency corresponds to shorter wavelength, ultimately resulting in denser meshing.

In comparison, IES is based on Multilevel Fast Multipole Method. It uses surface meshing to analyze

the frequency domain. The results of this solver contain information about the coupling between pairs of surface mesh elements. This process requires a lot of time and memory, but uses a MultiLevel Fast Multipole Method, which is advantageous for problems involving large structures. Otherwise stated, IES is particularly useful for simulations with big structures such as radio telescopes. Through tests with different set up, it was shown that IES is much more efficient for our purposes compared to the transient solver, especially when the dishes are rotated around the East-West axis to point at the NCP.

Due to the difference in approaches the Transient solver and the IES takes to solve the same problem, the Transient solver requires all the ports in the simulation to be excited to yield a correct result whereas IES does not. This is another reason why IES is more efficient for our simulation since there are 32 ports involved. Moreover, the presence of the horizontal-polarization ports matters to the simulation of the cross-coupling between the vertical-polarization ports. While all the other variables are controlled, the power cross-coupling simulated from the model with both the horizontal and vertical polarization ports present is about 15 to 20 decibel higher than the result from the simulation with the vertical polarization only. Consequently, we decide to use IES for our analysis of this problem, with a list of selected port excited.

Simulations of cross-coupling using CST can be time-consuming. The simulation time depends on different factors including the number of mesh cells. The size of our array is a circle of radius $\sim 20\,\mathrm{m}$ with 16 dishes. We use up to 15 cells per wavelength on the geometry and five in free space as our mesh setting, which results in roughly five million cells for the entire array (check the numbers). With the medium accuracy setting, 10^{-3} which is the default for the IES, this requires ~ 300 Gb of RAM. Memory is typically the limiting factor for the computation while using the IES. In our case, this is beyond the capacity of our lab computers that we collaborate with the Center for High Throughput Computing (CHTC) at the University of Wisconsin - Madison to perform the simulations. The advantage of using computing clusters like CHTC is that, in addition to gaining access to computers with higher RAM, one can run many jobs simultaneously, as licenses allow. In our case, we break down a simulation with 101 frequency samples to 101 simulations with a single frequency sample and run $10 \sim 15$ of them in parallel. The parallelization has helped us to reduce the total simulation time required to less than half of what would have taken if we used a single computer.

5.2. *Tests of S2,1 and S1,2 Symmetry*

One sanity check that one can perform to gain confidence on the CST simulation is the check of S2,1 and S1,2 symmetry. By symmetry, the response to port 2 to a signal from port 1 should be the same as the response of port 1 to the identical signal from port 2. Fig. 4 shows the result from our simulation, with a pair of dishes pointing at the zenith. From this, we concluded that CST simulation is quite reliable with our simulation settings. David: add numerical values for the accuracy.

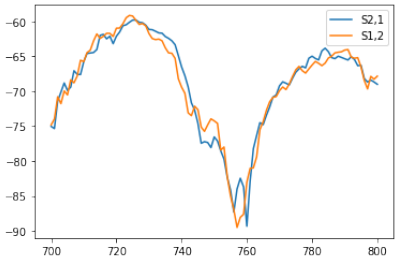

Fig. 4. Simulated S2,1 and S1,2 with a zenith-pointing pair of dishes.

We also simulate S2,1 and S1,2 with the full array of dishes pointing at the North Celestial Pole (Fig. 5), which is the configuration for the data taken. Here we see some disparities between curves. We think that this is due to the complexity of the geometry and the interactions between different elements of the array.

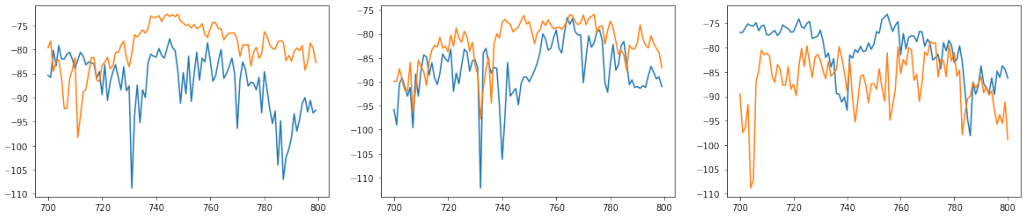

Fig. 5. caption

5.3. *Beam pattern simulations*

David: Do we need this here?

6. Correlated noise from cross-coupling of receiver noise (David)

6.1. *Noise model of receivers*

Rogers and Bowman (Rogers & Bowman, 2012) use the noise wave model of Meys (Meys, 1978) to estimate the noise emitted by the receiver toward the antenna in the EDGES global 21 cm spectrum instrument. We follow their approach closely and reproduce the analysis in App. B. Each LNA, labelled i, is characterized by three noise temperatures, T_{ui}, T_{corri}, and T_{0i}. T_{ui} is uncorrelated with the output of amplifier i. $T_0 i$ is uncorrelated with the input of amplifier i. Only $T_{corr} i$ introduces a correlation between the input and output of amplifier i.

6.2. *Cross-coupling model*

Figure 6 shows a schematic of the noise coupling model for the case of 3 antennas. The visibility for baseline 1-2 includes a cross-correlation between the T_{corr1} and itself as well as between T_{corr2} and itself. The visibility for baseline 2-3 contains similar terms from T_{corr2} and T_{corr3}, as well as an additional cross-correlation from the portions of $T_u 1$ and T_{corr1} that couple into antennas 2 and 3. Peter: Indicate that we are working only to first order in S.

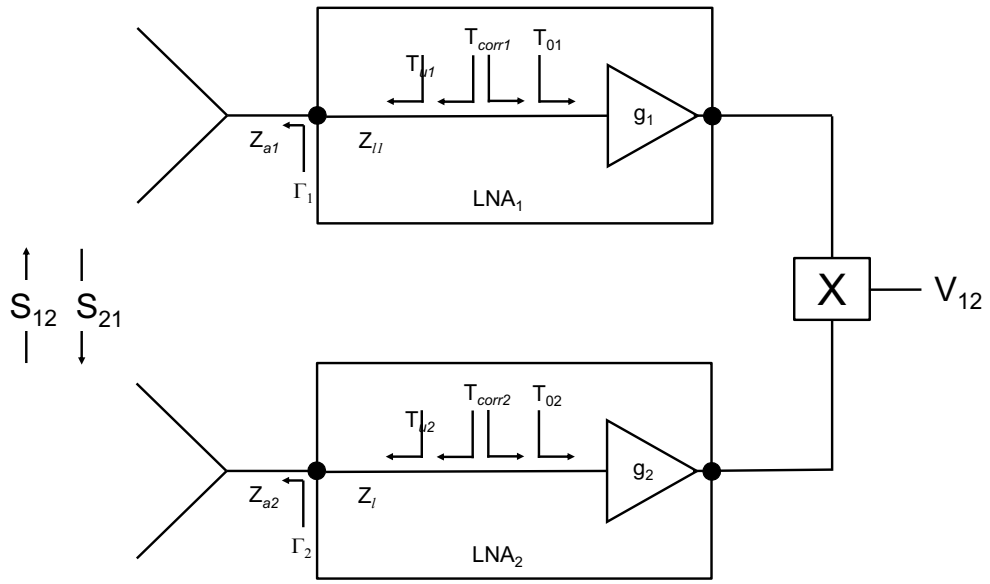

Fig. 6. Schematic of cross-coupling model for a pair of antennas. Independent noise temperatures T_u, T_{corr}, and T_0 are generated in the LNAs. Coupling between antenna 1 and antenna 2 is quantified by the (voltage) scattering parameter S_{12}. The visibility formed by correlating the pair of signals is V_{12}.

6.3. *Calculations S21 vs frequency for pairs of dishes embedded in 16TDPA*

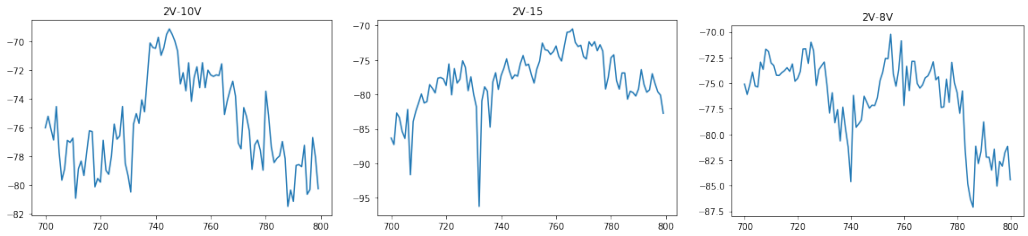

Fig. 7. Simulated S-parameters for the corresponding baselines. For the comparison of S21 and S12 of these baselines, see Fig. 5.

6.4. *Cross-Coupling Dependence on Baseline Length*

Simulations for pair of zenith-pointing *Dish Array* antennas; pairs of NCP-pointing antennas within *Dish Array*.

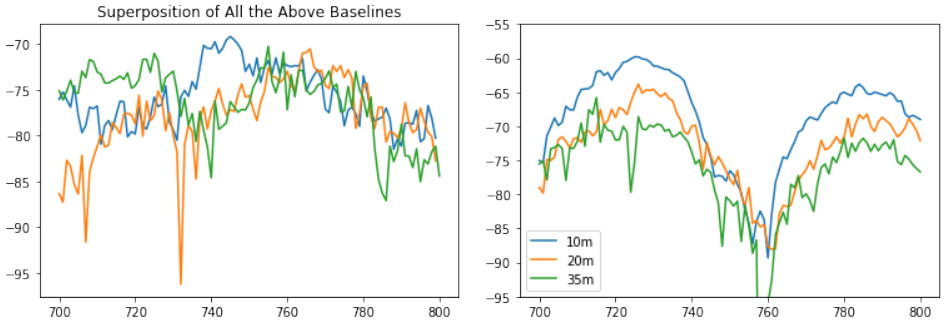

Fig. 8. **Right:** Superposition of all S-parameters in Fig. 7. When the entire array is present, the S-parameters do not show clear dependence on the baseline length. **Left:** Distance dependence of the S-parameters from a zenith-pointing pair

6.5. *Delay Spectrum Analysis (David & John)*

Delay spectrum analysis on the simulated crosstalk to check if we see the features that we expect
Attempt to calibrate crosstalk by comparing the simulated crosstalk in the delay spectrum with the signal in the delay spectrum and potentially subtracting the crosstalk from the signal

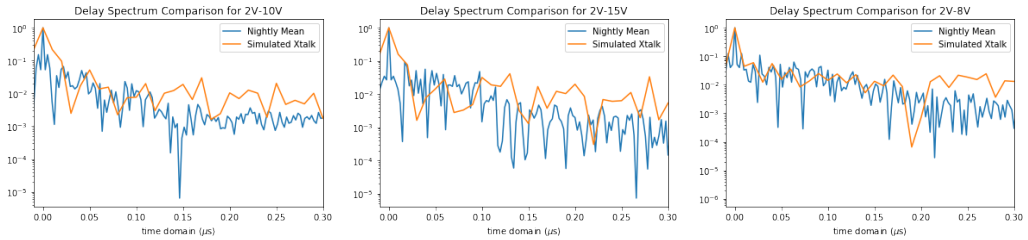

Fig. 9. Comparison of delay spectra of the nightly mean and that of the simulated crosstalk. Only half of the delay space is shown because the Fourier transform of real data is taken, which results in delays symmetric to the center. We suggest that the delays for the same baseline has similar structure; however, the frequency sample (101 bins over 700-800 MHz) is insufficient to compare the detail structure of one to the other.

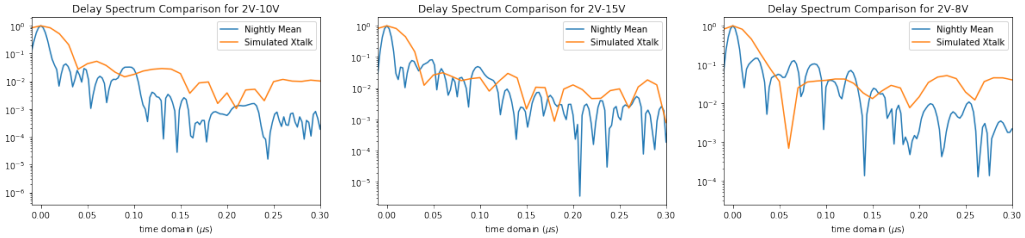

Fig. 10. Same delays with Blackman-Harris window applied twice

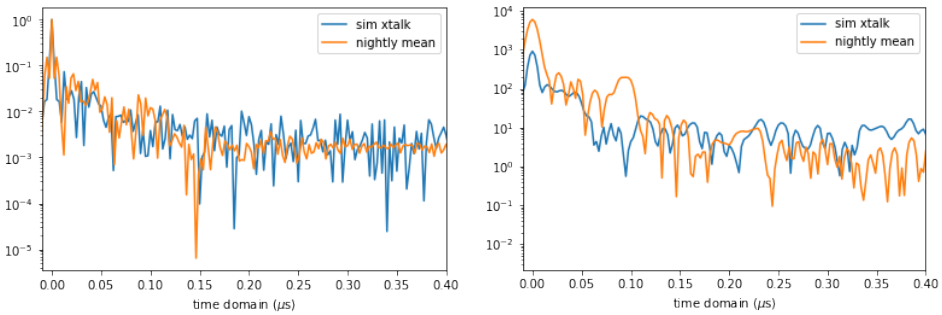

Fig. 11. **Right:** Delay of the 2V-10V pair with higher frequency sampling rate (401 bins over 700-800 MHz) superposed on the delay spectrum of the nightly mean for the baseline (410 bins over 700-800 MHz). Note that Fig. 10 is the simulation with the entire array present where as this is from the simulation with only a pair of dishes. **Left:** Same delays with Blackman-Harris window applied twice.

6.6. *Effect of ground on cross-coupling?*

Need to check this, but hopefully it's negligible. Haotian could do a wider range of frequencies with a pair of dishes and explore a range of ground models.

7. Correlated noise from thermal emission from the ground (Albert; Peter & David)

7.1. *Model for thermal emission from ground*

Haotian will insert a table of the complex permittivity (ϵ and $\epsilon\prime$) for a 'typical' soil with several different values of moisture content near 750 MHz, and two plots: **??** of emissivity vs angle of incidence for these different cases, one plot for each polarization. The latter plot is based on the Fresnel coefficients ϵ which should be defined in Appendix 1. (Sutinjo *et al.*, 2015) (Juswardy, 2022)

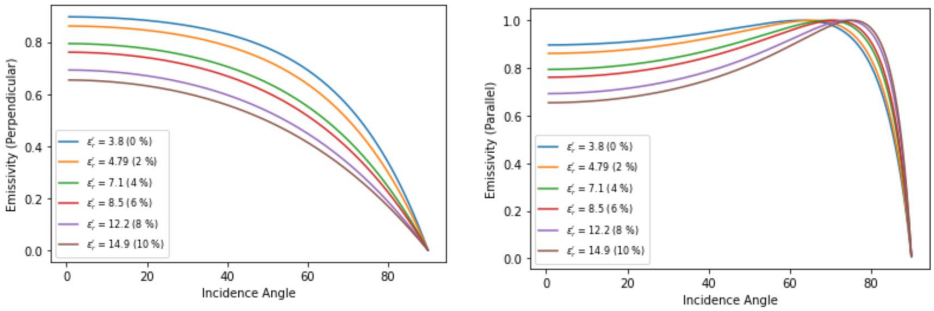

Fig. 12. Ground Emissivity for at 750 MHz from the MRO material; left: perpendicular polarized; right: parallel polarized

7.2. *Beam simulations*

To model the ground pickup for particular baselines accurately we need to simulate the beam patterns of the dish antennas that form a baseline as a function of frequency. 1 MHz sampling. Ideally, the simulations would include the full, 16 dish array because dishes interact with each other. In particular, some dishes block the beams of other dishes. Further, the beams are affected by reflections from the ground. Computing these effects for all pairs of antennas in the array would be costly, so we compute the beams for just a few pairs of antennas.

7.2.1. *Isolated dishes, pairs of dishes, dishes embedded in T16DPA*

To assess the tradeoffs of including the above effects, we evaluate beam patterns for a single antenna, a pair of antennas, and a pair of antennas embedded in the full array at a few frequencies (start with a single frequency, 750 MHz). In all cases, we consider two pointings of the antennas: toward the NCP and toward the zenith.

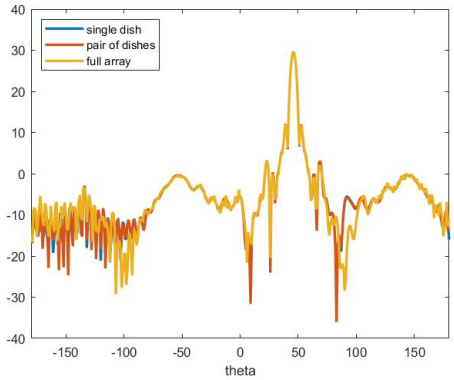

Fig. 13. Comparison of the beam patterns at 750 MHz of 15V by itself (blue), in pair (with dish 2; red), and with all the other dishes in the array (yellow). This is E-plane pattern.

7.2.2. *Effect of the ground on beam patterns*

For each of the cases in the previous section, we compare the case of no ground (antennas in free space) and with the ground.

Haotian is planning to co-plot a cut through the beams at 750 MHz for the case of the single dish and a pair of dishes, including the 4 ground permittivity models used in making Figs. A.1 and **??**.

8. Combined cross-coupling and ground emission model (David; Peter)

Waiting for ground results

8.1. *Expected visibilities from astronomical sources*

These are included in Figure 15. Peter will describe how Reza computed these.

8.2. *Comparison to measured correlated noise*

Plots from (Wu *et al.*, 2021).

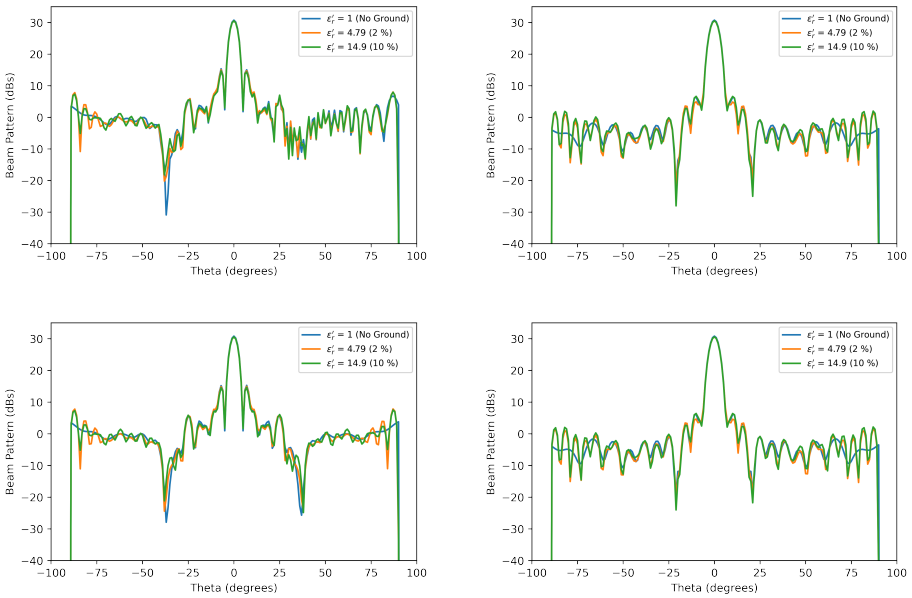

Fig. 14. Simulated directivity gain Peter: check this for a pair of dishes (top row) and a single (bottom row) dish for the $\phi = 0^\circ$ cut (E plane, first column) and the $\phi = 90^\circ$ cut (H plane, second column).

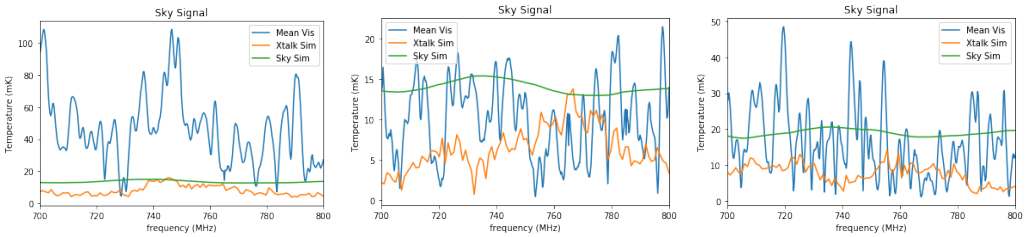

Fig. 15. Comparison of nightly mean, simulated sky, and simulated crosstalk for three different baselines.

8.3. *Delay spectrum?*

8.4. *Stability with time*

9. How to control these effects (John; David)

Improved antennas: simulated dish array with optimized feed and dish

David: blend this into conclusion?

10. Conclusion

future works: test with direct measurements

Acknowledgments

We are thankful to TBD for their constant support, constructive comments, and other contributions. The Tianlai array is operated with the support of NAOC Astronomical Technology Center. Work at UW-Madison and Fermilab is partially supported by NSF Award AST-1616554. Fermilab is operated by Fermi Research Alliance, LLC, under Contract No. DE-AC02-07CH11359 with the US Department of Energy. Work at UW-Madison is further supported by the Graduate School, the Thomas G. Rosenmeyer Cosmology Fund, and by a student award from the Wisconsin Space Grant. Work at NAOC is supported by MOST grants 2016YFE0100300 and 2012AA121701, 2018YFE0120800, the NSFC grant 11633004, 11473044, 11761141012, 11653003, 11773031, CAS grant QYZDJ-SSW-SLH017, XDA15020200. Part of

the computation is performed on the Tianhe-2 supercomputer with the support of NSFC grant U1501501. Authors affiliated with French institutions acknowledge partial support from CNRS (IN2P3 & INSU), Observatoire de Paris and from Irfu/CEA. This document was prepared by the Tianlai Collaboration includes personnel and uses resources of the Fermi National Accelerator Laboratory (Fermilab), a U.S. Department of Energy, Office of Science, HEP User Facility. Fermilab is managed by Fermi Research Alliance, LLC (FRA), acting under Contract No. DE-AC02-07CH11359.

Appendices

Appendix A Emissivity

below mostly copied from the optics textbook; needs revision later Emissivity of the surface of a material is usually referred to as the effectiveness in emitting energy as thermal radiation. Quantitatively, emissivity is the ratio of the thermal radiation from a surface to the radiation from an ideal black body at the same temperature as given by the Stefan-Boltzmann law, and the ratio is between 0 and 1 (Peatross et al, 2015).

Here, we study the emissivity of the ground area under the Tianlai dish array and see how much impact it has on the beam pattern received by the antennas.

Define θ_i as the incident angle and θ_t as the refracted angle, and n_1 as the incident index and n_2 as the refracted index (Peatross et al, 2015). Consider a planar boundary between two materials with different indices. When a plane wave traveling in the direction $\mathbf{k}_t$ is incident on the boundary from the left, it gives rise to a reflected plane wave traveling in the direction $\mathbf{k}_r$ and a transmitted plane wave traveling in the direction $\mathbf{k}_t$. The incident and reflected waves exist only to the left of the material interface, and the transmitted wave exists only to the right of the interface. The angles θ_i, θ_r, and θ_t give the angles that each respective wave vector ($\mathbf{k}_i$, $\mathbf{k}_r$, and $\mathbf{k}_r$) makes with the normal to the interface (Peatross & Ware, 2020).

The electric field vector for each plane wave is confined to a plane perpendicular to its wave vector. We are free to decompose the field vector into arbitrary components as long as they are perpendicular to the wave vector. It is customary to choose one of the electric field vector components to be that which lies within the plane of incidence. We call this p-polarized light, where p stands for parallel to the plane of incidence. The remaining electric field vector component is directed normal to the plane of incidence and is called s-polarized light. The s stands for senkrecht, a German word meaning perpendicular.

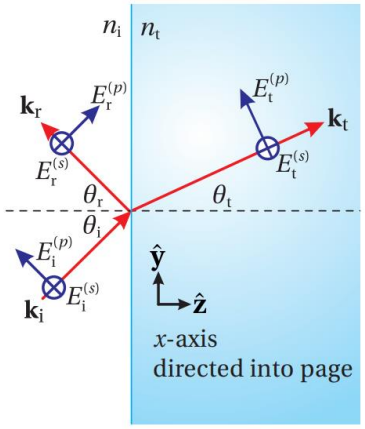

Fig. A.1. Incident, reflected, and transmitted plane wave fields at a material interface.

We first use the Fresnel coefficients for reflections with parallel r_s and perpendicular r_p polarization.

$$r_s = \frac{\sin\theta_t \cos\theta_i - \sin\theta_i \cos\theta_t}{\sin\theta_t \cos\theta_i + \sin\theta_i \cos\theta_t} \tag{A.1}$$

$$r_p = \frac{\sin\theta_t \cos\theta_t - \sin\theta_i \cos\theta_i}{\sin\theta_t \cos\theta_t + \sin\theta_i \cos\theta_i} \tag{A.2}$$

By Snell's law $n_1 \sin\theta_1 = n_2 \sin\theta_2$, we could reduce (A.1) to the following:

$$r_s = \frac{\frac{1}{n_2}\sin\theta_i \cos\theta_i - \alpha \sin\theta_i \cos\theta_i}{\frac{1}{n_2}\sin\theta_i \cos\theta_i + \alpha \sin\theta_i \cos\theta_i} \tag{A.3}$$

$$r_s = \frac{\sin\theta_i \cos\theta_i - n_2\alpha \sin\theta_i \cos\theta_i}{\sin\theta_i \cos\theta_i + n_2\alpha \sin\theta_i \cos\theta_i} \tag{A.4}$$

where α comes from the Fresnel equations:

$$\alpha = \frac{\cos t}{\cos i} \tag{A.5}$$

$$\alpha = \frac{\sqrt{1 - [(\frac{n_1}{n_2}\sin\theta_i)]^2}}{\cos\theta_i} \tag{A.6}$$

Given the relation between incident and refracted index and dielectric constant $n = \sqrt{\epsilon_r}$, we could reduce the formula to the following:

$$r_s = \frac{\sin\theta_i \cos\theta_i - \sqrt{\epsilon_r}\alpha \sin\theta_i \cos\theta_i}{\sin\theta_i \cos\theta_i + \sqrt{\epsilon_r}\alpha \sin\theta_i \cos\theta_i} \tag{A.7}$$

Also, the parallel polarization case gives:

$$r_p = \frac{\alpha \sin\theta_i \cos\theta_i - \sqrt{\epsilon_r}\sin\theta_i \cos\theta_i}{\alpha \sin\theta_i \cos\theta_i + \sqrt{\epsilon_r}\sin\theta_i \cos\theta_i} \tag{A.8}$$

Now, we want to know the fraction of power that reflects from or transmits through an interface. Energy conservation requires the incident power to balance the reflected and transmitted power:

$$P_i = P_r + P_t \tag{A.9}$$

We assume that transmittance is negligible. Moreover, the power separates cleanly into power associated with s-and p-polarized fields:

$$P_i^{(s)} = P_r^{(s)},\ P_i^{(p)} = P_r^{(p)} \tag{A.10}$$

Since the power is proportional to intensity and intensity is proportional to the square of the field amplitude. We could write the fraction of reflected power, reflectance, in terms of our previously defined Fresnel coefficients:

$$R_s \equiv \frac{P_r^{(s)}}{P_i^{(s)}} = \frac{I_r^{(s)}}{I_i^{(s)}} = \frac{|E_r^{(s)}|^2}{|E_i^{(s)}|^2} = |r_s|^2 \tag{A.11}$$

$$R_p \equiv \frac{P_r^{(p)}}{P_i^{(p)}} = \frac{I_r^{(p)}}{I_i^{(p)}} = \frac{|E_r^{(p)}|^2}{|E_i^{(p)}|^2} = |r_p|^2 \tag{A.12}$$

The sum of reflectance and emissivity should be equal to 1, hence the emissivity can be expressed:

$$\epsilon_s = 1 - R_s \tag{A.13}$$

$$\epsilon_p = 1 - R_p \tag{A.14}$$

Appendix B Noise emitted by receivers

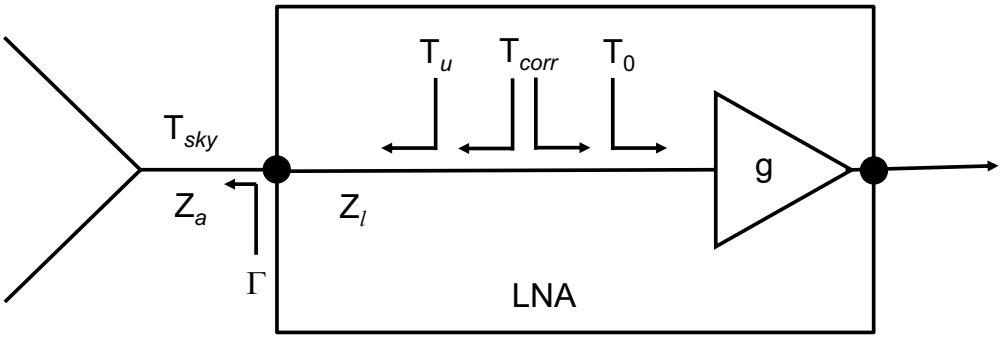

Fig. B.1. Schematic of noise model for a single antenna and low noise amplifier.

Rogers and Bowman(Rogers & Bowman, 2012) use the noise wave model of Meys(Meys, 1978) to estimate the noise emitted by the receiver toward the antenna in the EDGES global 21 cm spectrum instrument. We follow their approach closely here.

Fig. B.1 shows the circuit model for an antenna connected to a receiver. There is an impedance mismatch between the antenna and receiver. The antenna has impedance Z_a and collects a signal from the sky with a temperature, T_{sky}. The output of the antenna connects directly to the input of the receiver, which is modeled and a low noise amplifier (LNA) with an input impedance Z_l.

The reflection coefficient at the connection between the antenna and receiver, looking toward the antenna, is

$$\Gamma = \frac{Z_a - Z_l^*}{Z_a + Z_l}. \tag{B.1}$$

The LNA is modeled as a noiseless amplifier with power gain g and three "noise power wave" terms (Meys, 1978), all referred to the LNA input. T_0 is the noise temperature of a noise power wave traveling into the input of the LNA and is independent of the LNA input. T_u is the noise temperature of a noise power wave emitted by the LNA input and traveling to the left ("backwards") in the figure. T_u is uncorrelated with the noise at the output of the amplifier. In addition, T_{corr} represents two noise power waves that are correlated with each other; one travels to the left and one travels to the right.

A fraction of the uncorrelated and correlated noise waves is reflected at the interface with the antenna, with reflection coefficient Γ, back into the input of the LNA. The amount of T_u radiated by the antenna is $T_u(1 - |\Gamma|^2)$. We measured $T_{corr} \ll T_u$, so we neglect it for now.

Measuring the noise terms

In order to determine Γ, it is convenient to include in the circuit model a coaxial line of impedance $Z_0 = 50\,\Omega$ and zero length because the impedances and scattering parameters of the antenna and LNA are measured (with a VNA) and simulated (as described in section 5) with respect to a reference impedance of $50\,\Omega$. See Fig. B.2. In terms of the given impedances, the reflection coefficients Γ_a (looking into the antenna output) and Γ_l (looking into the LNA input) and a (complex) factor F are:

$$\Gamma_a = \frac{Z_a - 50}{Z_a + 50}, \tag{B.2}$$

$$\Gamma_l = \frac{Z_l - 50}{Z_l + 50}, \tag{B.3}$$

and

$$F = \frac{(1 - |\Gamma_l|^2)^{1/2}}{1 - \Gamma_a \Gamma_l}. \tag{B.4}$$

The receiver noise temperature, T_{rec}, for this system is given by Equation 8 of (Rogers & Bowman, 2012).

$$T_{rec} = T_{sky}(1 - |\Gamma_a|^2)|F|^2 + T_u|\Gamma_a|^2|F|^2 + (T_c \cos\phi + T_s \sin\phi)|\Gamma_a||F| + T_0 \tag{B.5}$$

The first term on the RHS represents the antenna temperature, T_a, at the input to the gain block after accounting for the impedance mismatch between the antenna and the LNA. Specifically,

$$T_a = T_{sky}(1 - |\Gamma|^2) = T_{sky}((1 - |\Gamma_a|^2)|F|^2. \tag{B.6}$$

Similarly, the second term on the RHS of Eq. B.5 is the fraction of the uncorrelated LNA noise that enters the LNA input after reflecting from the impedance mismatch between the LNA and the antenna. The third term is the corresponding reflected contribution from the correlated portion of the LNA noise. The reflected correlated noise interferes with correlated noise in the LNA with a relative phase angle ϕ. T_c and T_s are the coefficients of the cosine and sine parts, respectively, of the correlated wave. The noise temperature at the output of the LNA is then gT_{rec}.

These various LNA noise temperatures, T_u, T_c, T_s, and T_0, can be measured by measuring the power output of the LNA while terminating its input with 4 different loads: a 50 Ω load at two different temperatures, an open, and a short. These measurements are equivalent to replacing Z_a with different impedances. Specifically, the outputs are:

$$gT_{open} = \begin{cases} g(T_u + T_c + T_0) & (\phi = 0) \\ g(T_u - T_c + T_0) & (\phi = \pi) \end{cases}, \tag{B.7}$$

$$gT_{50\Omega,Hot} = g(T_{Hot} + T_0), \tag{B.8}$$

and

$$gT_{50\Omega,Cold} = g(T_{Cold} + T_0). \tag{B.9}$$

These equations can be solved for T_u, T_c, and T_0. T_s can be solved for by adding a line of length $\lambda/8$ to the open and short terminations.

Laboratory measurements

For the case of a Minicircuits ZFL-1000LN amplifier, using $T_{Hot} = 300\,\mathrm{K}$ and $T_{Cold} = 77\,\mathrm{K}$ we find $T_u = 129\,\mathrm{K}$, $T_c = 8.1\,\mathrm{K}$, and $T_0 = 664\,\mathrm{K}$. The expected noise temperature for this amplifier is 275 K.

Peter: Show simulated and measured Z_a for Tianlai dish feed and feed/dish. Can get this from S_{11}.

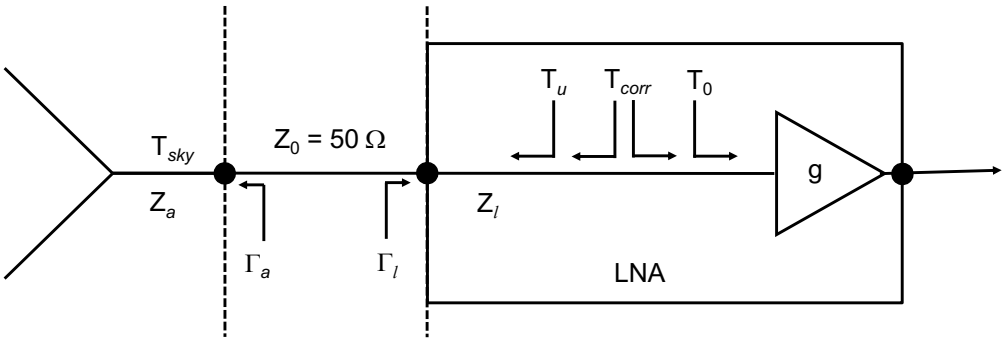

Fig. B.2. Schematic of noise model for a single antenna and low noise amplifier connected by a 50Ω coaxial line of zero length.

References

Fagnoni, N., de Lera Acedo, E., DeBoer, D. R., Abdurashidova, Z., Aguirre, J. E., Alexander, P., Ali, Z. S., Balfour, Y., Beardsley, A. P., Bernardi, G., Billings, T. S., Bowman, J. D., Bradley, R. F., Bull, P., Burba, J., Carilli, C. L., Cheng, C., Dexter, M., Dillon, J. S., Ewall-Wice, A., Fritz, R., Furlanetto, S. R., Gale-Sides, K., Glendenning, B., Gorthi, D., Greig, B., Grobbelaar, J., Halday, Z., Hazelton, B. J., Hewitt, J. N., Hickish, J., Jacobs, D. C., Josaitis, A., Julius, A., Kern, N. S., Kerrigan, J., Kim, H., Kittiwisit, P., Kohn, S. A., Kolopanis, M., Lanman, A., Plante, P. L., Lekalake, T., Liu, A., MacMahon, D., Malan, L., Malgas, C., Maree, M., Martinot, Z. E., Matsetela, E., Mena Parra, J., Mesinger, A., Molewa, M., Morales, M. F., Mosiane, T., Neben, A. R., Nikolic, B., Parsons, A. R., Patra, N., Pieterse, S., Pober, J. C., Razavi-Ghods, N., Robnett, J., Rosie, K., Sims, P., Smith, C., Syce, A., Thyagarajan, N., Williams, P. K. G. & Zheng, H. [2021] **500**, 1232, doi:10.1093/mnras/staa3268.

Josaitis, A. T., Ewall-Wice, A., Fagnoni, N. & de Lera Acedo, E. [2022] **514**, 1804, doi:10.1093/mnras/stac916.

Juswardy, B. [2022] personal communication.

Kern, N. S., Parsons, A. R., Dillon, J. S., Lanman, A. E., Fagnoni, N. & de Lera Acedo, E. [2019] **884**, 105, doi:10.3847/1538-4357/ab3e73.

Kern, N. S., Parsons, A. R., Dillon, J. S., Lanman, A. E., Liu, A., Bull, P., Ewall-Wice, A., Abdurashidova, Z., Aguirre, J. E., Alexander, P., Ali, Z. S., Balfour, Y., Beardsley, A. P., Bernardi, G., Bowman, J. D., Bradley, R. F., Burba, J., Carilli, C. L., Cheng, C., DeBoer, D. R., Dexter, M., de Lera Acedo, E., Fagnoni, N., Fritz, R., Furlanetto, S. R., Glendenning, B., Gorthi, D., Greig, B., Grobbelaar, J., Halday, Z., Hazelton, B. J., Hewitt, J. N., Hickish, J., Jacobs, D. C., Julius, A., Kerrigan, J., Kittiwisit, P., Kohn, S. A., Kolopanis, M., La Plante, P., Lekalake, T., MacMahon, D., Malan, L., Malgas, C., Maree, M., Martinot, Z. E., Matsetela, E., Mesinger, A., Molewa, M., Morales, M. F., Mosiane, T., Murray, S. G., Neben, A. R., Parsons, A. R., Patra, N., Pieterse, S., Pober, J. C., Razavi-Ghods, N., Ringuette, J., Robnett, J., Rosie, K., Sims, P., Smith, C., Syce, A., Thyagarajan, N., Williams, P. K. G. & Zheng, H. [2020] **888**, 70, doi:10.3847/1538-4357/ab5e8a.

Meys, R. P. [1978] *IEEE Transactions on Microwave Theory Techniques* **26**, 34, doi:10.1109/TMTT.1978.1129303.

Padin, S., Cartwright, J. K., Joy, M. & Meitzler, J. C. [2000] *IEEE Transactions on Antennas and Propagation* **48**, 836, doi:10.1109/8.855504.

Padin, S., Shepherd, M. C., Cartwright, J. K., Keeney, R. G., Mason, B. S., Pearson, T. J., Readhead, A. C. S., Schaal, W. A., Sievers, J., Udomprasert, P. S., Yamasaki, J. K., Holzapfel, W. L., Carlstrom, J. E., Joy, M., Myers, S. T. & Otarola, A. [2002] **114**, 83, doi:10.1086/324786.

Peatross, J. & Ware, M. [2020] *Physics of Light and Optics* (Brigham Young University), https://optics.byu.edu/docs/opticsBook.pdf.

Rogers, A. E. E. & Bowman, J. D. [2012] *Radio Science* **47**, RS0K06, doi:10.1029/2011RS004962.

Sun, S., Li, J., Wu, F., Timbie, P., Ansari, R., Geng, J., Shi, H., Stebbins, A., Wang, Y., Zhang, J. & Chen, X. [2022] *Research in Astronomy and Astrophysics* **22**, 065020, doi:10.1088/1674-4527/ac684d.

Sutinjo, A. T., Colegate, T. M., Wayth, R. B., Hall, P. J., de Lera Acedo, E., Booler, T., Faulkner, A. J., Feng, L., Hurley-Walker, N., Juswardy, B., Padhi, S. K., Razavi-Ghods, N., Sokolowski, M., Tingay, S. J. & de Vaate, J. G. B. [2015] *IEEE Transactions on Antennas and Propagation* **63**, 5433, doi:10.1109/tap.2015.2487504, URL https://doi.org/10.1109%2Ftap.2015.2487504.

Wu, F., Li, J., Zuo, S., Chen, X., Das, S., Marriner, J. P., Oxholm, T. M., Phan, A., Stebbins, A., Timbie, P. T., Ansari, R., Campagne, J.-E., Chen, Z., Cong, Y., Huang, Q., Kwak, J., Li, Y., Liu, T., Liu, Y., Niu, C., Osinga, C., Perdereau, O., Peterson, J. B., Podczerwinski, J., Shi, H., Siebert, G., Sun, S., Tian, H., Tucker, G. S., Wang, Q., Wang, R., Wang, Y., Wu, Y., Xu, Y., Yu, K., Yu, Z., Zhang, J., Zhang, J. & Zhu, J. [2021] **506**, 3455, doi:10.1093/mnras/stab1802.